

Simulation and Analysis of Event Camera Data for Non-Resolved Objects

Conor J. Benson and Marcus J. Holzinger

University of Colorado Boulder, Boulder, CO USA

ABSTRACT

Photon counters and exposure-based cameras cannot simultaneously provide exquisite temporal and spatial resolution in one sensor. Event (i.e. neuromorphic) cameras provide both and promise to advance studies of high-speed temporal and spatial intensity variations. Potential space domain awareness (SDA) applications include streak-based orbit determination and high frequency light curve analysis. No dynamic event camera simulations for non-resolved objects have been conducted. In this work, we develop an event camera model for this purpose. Referencing the event camera literature, we approximate the event pixel dynamics as a first order differential equation driven by logarithmic photon flux. The photon arrivals are modeled as a stochastic Poisson process. Considering static point sources with constant and time-varying mean brightness as well as moving sources, we use this model to explore event data dependencies on various target and sensor parameters. These parameters include the target's mean brightness, on-sky motion rate, the brightness amplitude and frequency as well as the event threshold and event circuit parameters. For the time-varying brightness case, we also study how frequency estimate signal-to-noise depends on these parameters. We then validate simulation results against real event data of non-resolved space objects, showing clear consistencies. The observed sensitivity to target parameters demonstrates the great potential of event cameras for high spatio-temporal resolution astrometry and photometry. Finally, we conduct frequency analysis on the real data.

1. INTRODUCTION

Unlike traditional frame-based exposure cameras, event cameras (also known as neuromorphic cameras) react to relative changes in brightness at the pixel level [5, 8]. Upon reaching a prescribed relative brightness change, a given pixel outputs an event, independent of all other pixels. As a result, event cameras react naturally to changes in the scene rather than being limited to a fixed frame-rate. Events are tagged with microsecond time resolution, yielding kHz or better single-pixel event rates accounting for post-event pixel reset times. Also, by operating on logarithmic intensities, event cameras are sensitive to relative changes in brightness over roughly 10 orders of magnitude. Furthermore, with events only produced when the brightness changes, event cameras have a greatly reduced data rate compared to traditional cameras with equivalent frame-rates. Overall, these attributes make event cameras particularly suited to studying high-rate temporal and spatial brightness variations for resident space objects (RSOs).

For example, event cameras could be used to provide finer astrometric information for fast-moving RSOs. Given their high temporal resolution and event polarity, event cameras are not subject to the direction of motion ambiguity of exposure-based streaks. These cameras could also improve studies of RSO structural vibration frequencies. With vibrational modes tied directly to RSO-specific structural properties and excitation mechanisms (e.g. reaction wheels, thruster firings, and non-principal axis tumbling), frequency estimates could be used to characterize (and possibly uniquely identify) objects and determine whether they are active or defunct. Further aiding characterization and identification, event-based data might also be used to detect micro-glint frequencies for uniform rotators to infer surface roughness (e.g. multi-layer insulation crinkles and tessellated solar arrays).

With event cameras providing low latency and data rates, most studies of event-based data have involved the broad fields of robotic vision and motion/pose estimation [5]. These applications often focus on feature and edge detection for resolved objects in relatively bright scenes. This is notably different from the SDA scenario where targets are generally dim, non-resolved, and subject to significant photon shot noise. So far, studies of event camera data for SDA have been limited mostly to observational demonstrations [2, 3]. Studies of event camera limiting magnitudes have been conducted, but assume an object has constant brightness and moves slowly across the field of view [9]. To our knowledge, no public literature exists on dynamic simulation of event camera data for non-resolved objects. High speed photon counter photometry has been explored for RSO structural mode inference (e.g. [14]), but event cameras

operate in a fundamentally different way with a stream of brightness change events rather than an explicit photon time history. The spatial resolution of event cameras and its potential to enhance both astrometric and photometric estimates also warrants further study. For example, with multiple independent pixels underlying a target's time-varying point spread function (PSF), the stochastically staggered events could enhance temporal resolution given non-zero pixel reset times.

Given the above discussion, the primary goal of this work is to advance understanding of event-based data for non-resolved objects. Starting from the event camera literature, we develop an event camera model driven by stochastic photon arrivals. With the model framework in place, we then apply it to the single and multi-pixel cases, considering static point sources, moving points sources, and sources with time-varying brightness. We explore how the resulting event data depends on a wide array of target and sensor parameters. For the target, these parameters include: the mean brightness, brightness variation amplitude and frequency as well as on-sky motion rates. For the sensor, these parameters include: the telescope aperture size, the event camera pixel size, event detection threshold, and event circuit parameters. We then explore how frequency estimate signal to noise depends on these target and sensor parameters. Finally, we validate simulation results using real event-based data of natural and artificial space objects and conduct frequency analysis on this real data.

2. EVENT CAMERA SIMULATION FRAMEWORK

Fundamentally, event camera pixels convert the natural logarithm of the photon flux into a voltage [8]. The common assumption is that the steady state voltage changes instantaneously to match the time-varying flux. We relax this assumption by modeling the voltage dynamics with a first order differential equation. We also assume the photon arrivals are stochastic and follow a Poisson process, defining $\lambda(t)$ as the corresponding Poisson rate (i.e. mean photon flux) for a given pixel. Each pixel's voltage $V(t)$ is modeled independently using the following differential equation,

$$\frac{dV(t)}{dt} = -aV(t) + h(t)p(t) \quad (1)$$

where a is the voltage decay rate, $h(t)$ is a scaling factor, and $p(t)$ is the stochastic photon impulse train which we define as the following summation of Dirac δ functions,

$$p(t) = \sum_{n=1}^{\infty} \delta(t - T_n) \quad (2)$$

where T_n is the stochastic arrival time of photon n . So for this model, each photon arrival causes an impulsive jump in voltage.

We define $h(t)$ as,

$$h(t) = b \frac{(\ln \lambda(t) - \ln \lambda_r)}{\lambda(t)} \quad (3)$$

where b is the constant gain and λ_r is the constant reference flux. Here, $(\ln \lambda(t) - \ln \lambda_r)/\lambda(t)$ scales the impulsive voltage jumps logarithmically with $\lambda(t)$.

We can analytically solve Eq. 1 (using Laplace transforms for example) to obtain,

$$V(t) = V_0 e^{-at} + \sum_{n=1}^{\infty} h(T_n) u(t - T_n) e^{-a(t-T_n)} = V_0 e^{-at} + \sum_{n=1}^{m(t)} h(T_n) e^{-a(t-T_n)} \quad (4)$$

where V_0 is the voltage at $t = 0$, $u()$ is the Heaviside unit step function, and $m(t)$ is the maximum n that satisfies $t < T_n$. In other words, $m(t)$ is the number of photons that have arrived by time t . So $V(t)$ is known provided we can simulate the random T_n values. Approaches for calculating these arrival times are presented in the following sections.

To compute events, the voltage $V(t)$ is compared with a reference value V_{ref} . When the voltage difference reaches either the positive (c_+) or negative (c_-) threshold (which can be different), an event with the corresponding polarity (+1 or -1) is declared and V_{ref} is set to $V(t)$. For clarity, note that λ_r is not related to event detection and remains fixed. In this work, we set c_{\pm} according to Eq. 9 in terms of the corresponding relative change in brightness $\Delta \bar{\lambda}$ (e.g. 10%).

$$V(t) - V_{\text{ref}} = c_{\pm} = \frac{b}{a} \ln(1 \pm \Delta\bar{\lambda}) \quad (5)$$

It is also valuable to derive analytical statistics for the voltage. We can equivalently write Eq. 1 as the following stochastic differential equation:

$$dV(t) = -aV(t)dt + h(t)dN_{\lambda}(t) \quad (6)$$

where the Poisson random variable $dN_{\lambda}(t)$ is the stochastic number of new photon arrivals at time t .

Taking the expectation of Eq. 6 and noting that $E[dN_{\lambda}(t)] = \lambda(t)dt$, we obtain the deterministic differential equation for the mean voltage,

$$\frac{d(E[V(t)])}{dt} = -aE[V(t)] + b \ln(\lambda(t)/\lambda_r) \quad (7)$$

2.1 Constant Mean Photon Flux λ

When $\lambda(t)$ is constant, the arrival times T_n can be modeled as a Homogeneous Poisson Process (HPP). In this case, T_n is given by,

$$T_n = \sum_{k=1}^n t_k \quad (8)$$

where the t_k 's are independently drawn from an exponential distribution with rate λ [4]. Eqs. 4, 5, and 8 can then be used to numerically simulate the event circuit for this constant λ case.

With $\lambda(t)$ constant, we can easily solve Eq. 7. Assuming $E[V_0] = E[V(t)]_{t \rightarrow \infty}$, we find that the mean voltage is,

$$E[V(t)] = \frac{b \ln(\lambda/\lambda_r)}{a} \quad (9)$$

Using Ito's chain rule for stochastic differential equations, we can obtain higher order moments. The steady-state voltage standard deviation is,

$$\sigma_V = \frac{b |\ln(\lambda/\lambda_r)|}{\sqrt{2a\lambda}} \quad (10)$$

2.2 Time-varying $\lambda(t)$

When $\lambda(t)$ is time-varying, the T_n 's must now be modeled as a Non-Homogeneous Poisson Process (NHPP). To do this, we use the Acceptance-Rejection (thinning) method [11]. The simplest form of Acceptance-Rejection (and the one used in this work) first simulates inter-arrival times for an HPP with constant rate λ_c where $\lambda_c \geq \lambda(t)$ for all time. These HPP arrivals are then removed with probability $1 - \lambda(\tau)/\lambda_c$ where τ is an arrival time from the HPP. The thinned arrivals then constitute an NHPP with rate $\lambda(t)$.

We will now consider the case where $\lambda(t)$ is given by,

$$\lambda(t) = \lambda_0 + \lambda_1 \sin \omega t \quad (11)$$

to model time-varying target brightness due to target rotation, vibration, etc. at the constant frequency ω .

We will consider analytical solutions for the mean voltage using Eq. 7 with $\lambda(t)$ given by Eq. 11:

$$\frac{d(E[V(t)])}{dt} = -aE[V(t)] + b \ln((\lambda_0 + \lambda_1 \sin \omega t)/\lambda_r) \quad (12)$$

To our knowledge, there is no exact closed form analytical solution to this differential equation. So we approximate $\ln(1 + \lambda_1/\lambda_0 \sin \omega t)$ with a Taylor series expansion in λ_1/λ_0 (the relative amplitude). Note that $\lambda(t) \geq 0$, so $\lambda_1/\lambda_0 \leq 1$. At second order, we have,

$$\ln\left(1 + \frac{\lambda_1}{\lambda_0} \sin \omega t\right) \approx \frac{\lambda_1}{\lambda_0} \sin \omega t - \left(\frac{\lambda_1}{\lambda_0}\right)^2 \sin^2 \omega t \quad (13)$$

With this approximation, we can solve Eq. 12. Neglecting the exponential terms (which will quickly decay to zero), the steady state mean voltage under the assumption of small λ_1/λ_0 is given by,

$$E[V(t)]_{ss} \approx \frac{b}{a} \left[\ln\left(\frac{\lambda_0}{\lambda_r}\right) + \frac{\lambda_1}{\lambda_0} \frac{\sin \omega t - \frac{\omega}{a} \cos \omega t}{1 + \frac{\omega^2}{a^2}} + \frac{1}{2} \frac{\lambda_1^2}{\lambda_0^2} \left(\frac{\cos 2\omega t + 2\frac{\omega}{a} \sin 2\omega t}{1 + 4\frac{\omega^2}{a^2}} - 1 \right) \right] \quad (14)$$

When we consider that the voltage event thresholds c_{\pm} are proportional to b/a , the only factors in $E[V(t)]_{ss}$ that dictate the number of events per cycle are λ_1/λ_0 and ω/a .

3. SIMULATION RESULTS

3.1 Constant λ

Figure 1 shows single pixel event camera results obtained by numerically simulating Eqs. 4 and 8. Figure 1a shows the voltage time histories for different λ values. For each case, V_0 is set to the analytically computed mean value from Eq. 9 (denoted by the solid black lines). The distance between the solid and each dashed black line are the c_{\pm} event threshold increments. First of all, we see that the runs track the mean values in all three cases. Crucially for the corresponding event rates, the voltage standard deviation σ_V varies notably with λ . In Figure 1b, the mean event rates are plotted vs. λ . Here, the event rate peaks for intermediate λ and approaches zero for extremal values. For small λ values, the voltage amplitude is large (see Eq. 10 where $\sigma_V \rightarrow \infty$ as $\lambda \rightarrow 0$). Nevertheless, the voltage is dominated by exponential decay with very few positive events (compare the positive and negative event rates in Figure 1b). So the event rate is limited by the circuit decay rate. For large λ values, the voltage fluctuates rapidly but the amplitude is small due to small relative variation in flux (again see Eq. 10 as $\lambda \rightarrow \infty$). So few events are triggered. Finally, for intermediate λ values, the voltage fluctuates quickly with significant amplitude, resulting in the highest event rates.

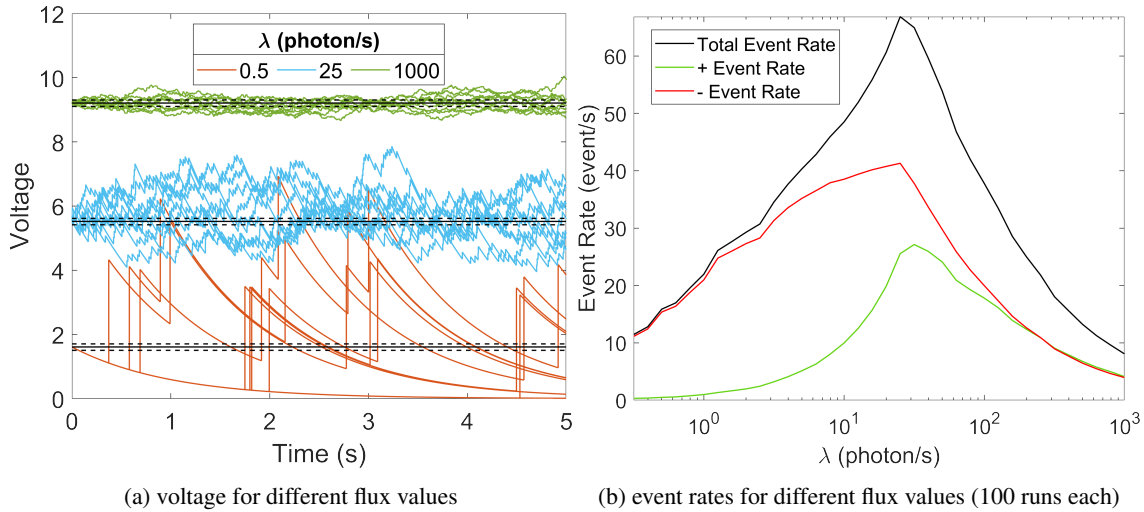


Fig. 1: Single pixel event camera simulation with constant mean flux λ , $a = b = 1$, $\lambda_r = 0.1$, $\Delta\bar{\lambda} = 0.1$

Figure 2 shows the total event rates as a function of the event circuit parameters a , b , λ_r , and $\Delta\bar{\lambda}$. When varying one parameter, the others are held at $a = b = 1$, $\lambda_r = 0.1$, $\Delta\bar{\lambda} = 10\%$. The rates increase significantly as a increases. Most importantly, the λ value corresponding to the peak event rate increases as a increases. Taking the ratio of σ_V to the event thresholds c_{\pm} (a good indicator of relative variation), we see that it is proportional to \sqrt{a} . Higher a will also result in faster voltage decay and more events per second. Interestingly, the intensity gain b has no effect on the event rate for the constant mean flux case. Considering again σ_V/c_{\pm} , we see that b cancels out. So even though increasing b increases the impulsive voltage change for each photon arrival in Eq. 1, b scales the event threshold equivalently. Next, the event rate increases as the reference flux λ_r is lowered. We see that σ_V increases as λ_r decreases. Finally, considering the brightness change threshold $\Delta\bar{\lambda}$, lower thresholds naturally generate more events.

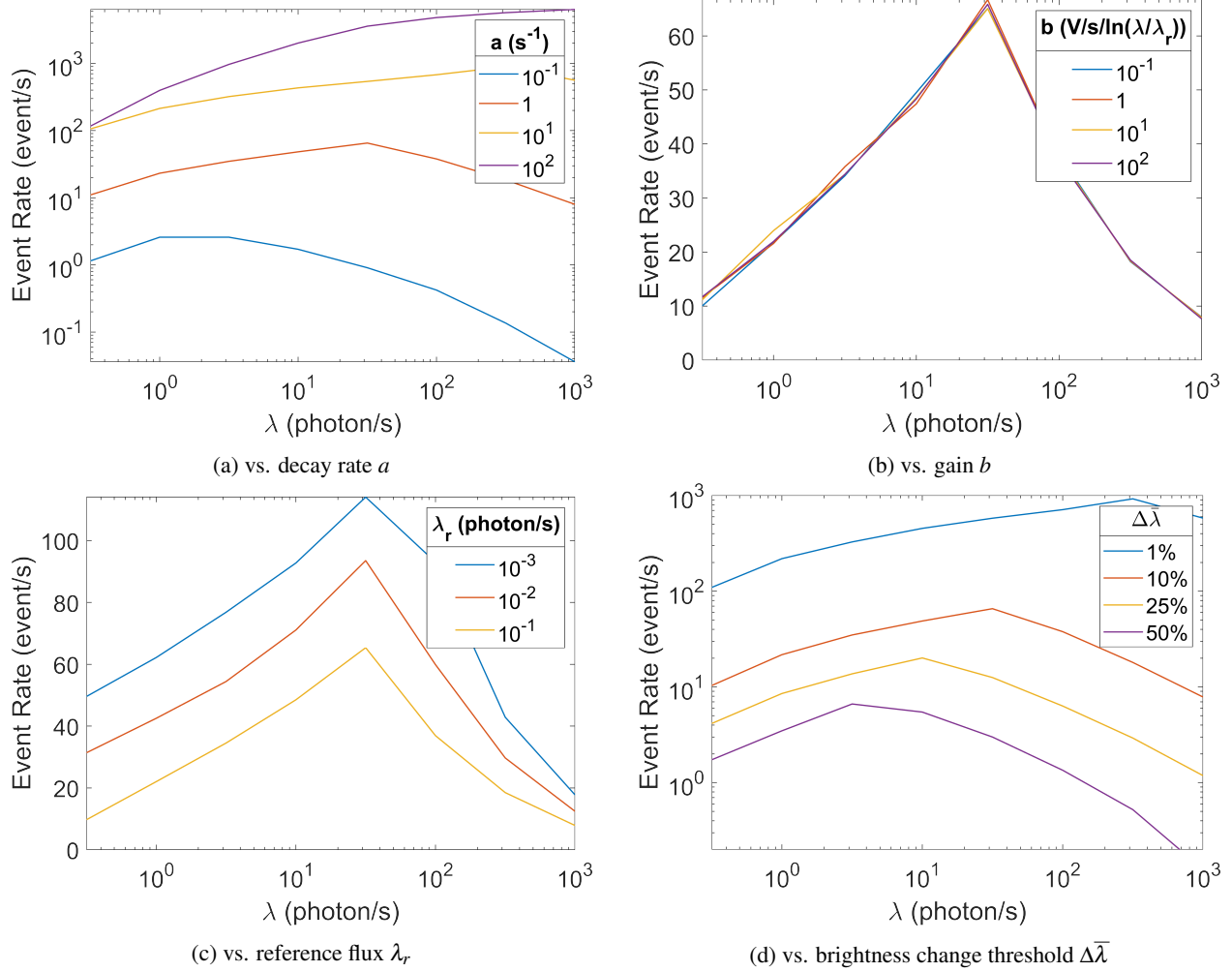


Fig. 2: Single pixel mean event rates vs. event circuit parameters over 100 runs

We can also explore multi-pixel event camera simulations. We model the target's point spread function (PSF) as a 2-D Gaussian and compute the mean photon flux λ_{ij} in pixel (i, j) using the error function as follows,

$$\lambda_{ij} = \frac{\Phi}{4} \left(\operatorname{erf} \hat{x}_{ij}^+ - \operatorname{erf} \hat{x}_{ij}^- \right) \left(\operatorname{erf} \hat{y}_{ij}^+ - \operatorname{erf} \hat{y}_{ij}^- \right) \quad (15)$$

where Φ is the total photon flux (photon/s) reaching the focal plane and the normalized pixel bounds are $\hat{x}_{ij}^\pm = \frac{1}{\sqrt{2}\sigma} (x_{ij}^\pm - \bar{x})$ and $\hat{y}_{ij}^\pm = \frac{1}{\sqrt{2}\sigma} (y_{ij}^\pm - \bar{y})$. Here (\bar{x}, \bar{y}) is the PSF centroid location and σ is the standard deviation ($\sigma = 0.45\Lambda N$ for diffraction limited observations where Λ is the mean wavelength of the event camera's sensitivity range and N is the telescope f-number). Practically, σ is larger due to atmospheric seeing. For a seeing disc with full width at half max FWHM, $\sigma = \text{FWHM}/\sqrt{8 \ln 2}$. With λ_{ij} computed, we independently simulate each pixel.

Figure 3a shows the event output for a 5 visible magnitude (m_v) diffraction-limited point source along with the corresponding point spread function in Figure 3b. Computing the photon irradiance from the approximate m_v relationship provided in Ref. [13], the Figure 3 results assume a 0.2 m aperture f/3 telescope with an IFOV of 0.18 arcsec/pixel. We also assume 50% atmospheric transmittance and a sky background brightness [1] of $18.6 m_v/\text{arcsec}^2$ (an approximate average from Clear Dark Sky for Boulder, Colorado). Figure 3a shows that the event rate at the PSF centroid is nearly zero due to small voltage variation for large λ_{ij} . Moving radially outward, the event rate increases as λ_{ij} decreases. The event rate then peaks before decreasing to the background noise. This behavior is consistent with the trend in Figure 1b. The overall event rate structure can be described as a central "depression" with a raised "rim". This structure is essentially the inverse of the PSF. We should note that the assumed sensor system would require a pixel size

of $\sim 0.5 \mu\text{m}$ (about an order of magnitude smaller than any commercially available event camera). So for the above telescope with an off the shelf camera, the event depression would only consist of a handful of pixels. Nevertheless, angular resolution similar to Figure 3 could be obtained with a $\sim 6 \text{ m}$ focal length telescope and commercially available camera. For reasonable f-numbers, this focal length would result in a large aperture, making the high photon rates computationally prohibitive with our current approach. However, the event rates can be inferred from the PSF alone. With higher flux at the centroid and the λ value for the peak event rate moving outward, the event depression would be deeper and wider for the same m_v .

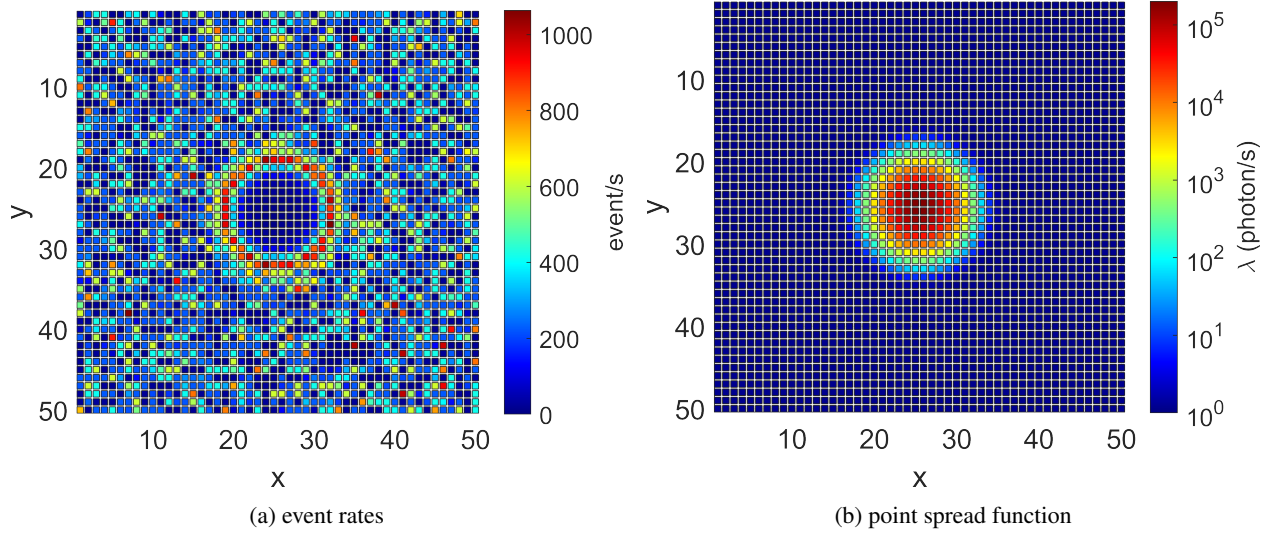


Fig. 3: Event camera simulation of stationary $5 m_v$ point source with $a = 10$, $b = 100$, $\Delta\bar{\lambda} = 10\%$

Expanding on the Figure 3 results with the same sensor system parameters, Figure 4 shows the event rates for point sources with varying visual magnitudes along with their corresponding PSFs. Here we display a cross-section through the PSF centroid. As the source brightness decreases (increasing m_v), the event depression becomes less pronounced and the rims move inward. At $\geq 12 m_v$, all pixel fluxes are to the left of the event rate peak from Figures 1 and 2. So the rims merge, and the event structure shrinks for progressively dimmer sources.

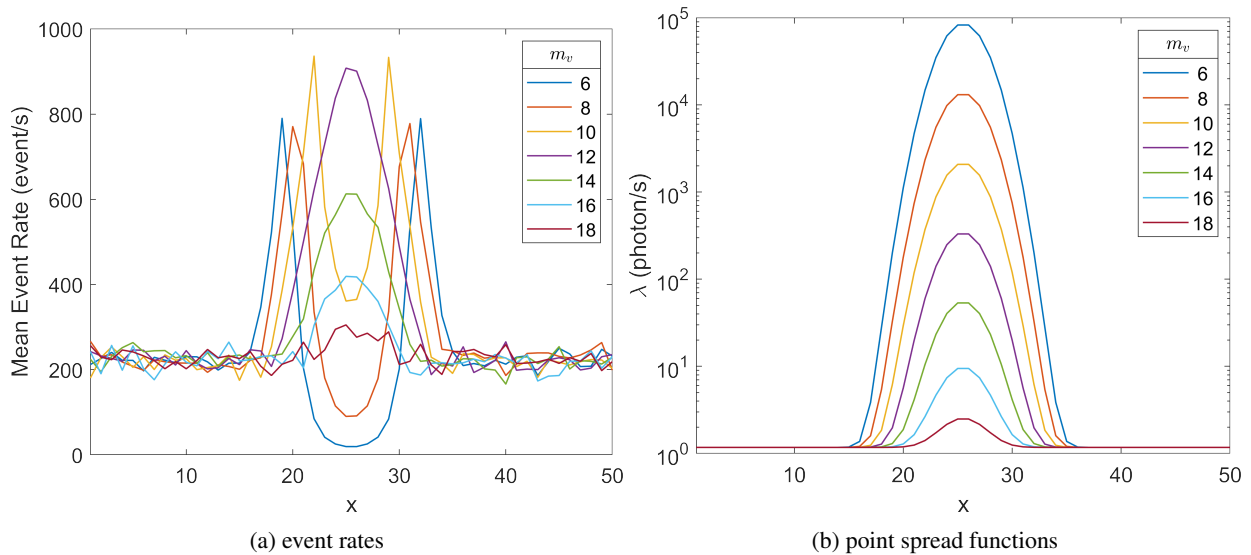


Fig. 4: Event rates across the center of the PSF for different magnitudes with $a = 10$, $b = 100$, $\lambda_r = 0.1$, $\Delta\bar{\lambda} = 10\%$

3.2 Sinusoidal $\lambda(t)$

An important question is how well event time histories capture sinusoidal flux variation. To address this, we will explore how frequency estimates depend on the target and circuit parameters. Figure 5 shows event frequency analysis for a 10 Hz sinusoidal $\lambda(t)$ with $\lambda_0 = 1000$ photon/s and $\lambda_1/\lambda_0 = 0.75$. This corresponds to a magnitude variation of $\Delta m = 2.5 \log_{10} \left(\frac{1+\lambda_1/\lambda_0}{1-\lambda_1/\lambda_0} \right) \approx 2$. Three cases are considered with different decay rate (a) values. The left plot of each row is the voltage calculated with Eq. 4. Since $\lambda(t)$ is time-varying, we simulate the photon arrivals as an NHPP using Acceptance-Rejection with $\lambda_c = \lambda_0 + \lambda_1$. In each voltage plot, the grey lines denote the ensemble of 100 runs per case. The yellow line highlights one of the runs. The black line is the mean voltage at a given time over all 100 runs. Finally, the purple line is the expected steady state voltage $E[V(t)]_{ss}$ given by Eq. 14. All runs are initialized at $V(t=0) = E[V(t=0)]_{ss}$. The middle plot on each row is the mean event over the 100 runs. If no event occurs at a given time step, we set the event to 0. The right plots show the normalized FFTs of the event time histories using an FFT integration time of 4.5 s (i.e. 45 cycles). For clarity, we only show the first 1 s of the voltage and event histories.

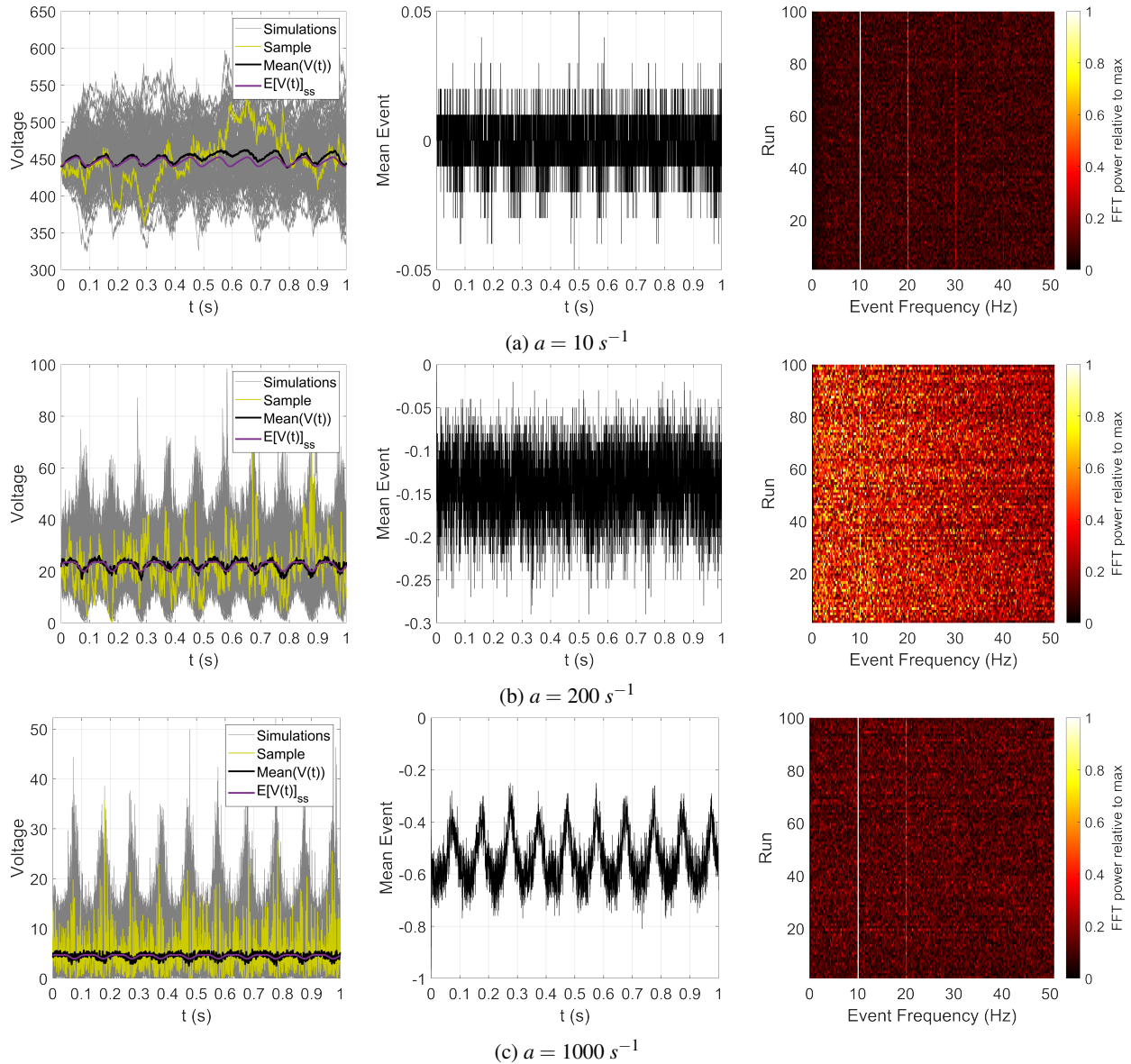


Fig. 5: Event frequency analysis for 10 Hz $\lambda(t)$ sinusoid with $\lambda_0 = 1000$ photon/s, $\lambda_1/\lambda_0 = 0.75$ ($\Delta m \sim 2$), $b = 500$, $\Delta\lambda = 10\%$, 100 runs each

There are several notable takeaways from Figure 5. First of all, we see that $E[V(t)]_{ss}$ closely tracks the computed mean voltage in each case. We also see that the frequency signal to noise varies considerably with a . Looking first at the $a = 10 \text{ s}^{-1}$ case, we see that the 10 Hz signal and several harmonics are clearly visible. The 0.1 s periodicity is also visible in the mean event data. As we increase a to 200 s^{-1} , the 10 Hz signal is almost completely washed out. It is also hard to see periodicity in the mean events. Interestingly, as we increase a to 1000 s^{-1} , the 10 Hz signal reappears clearly in the FFT and mean event data. This trend in a was observed for other λ_0 values as well. This behavior is analogous to that shown in Figure 2 where the noise-driven event rates are maximized for intermediate λ values. Here the noise-driven events are maximized for intermediate a values.

To set up our remaining discussion of frequency estimation, Figure 6 shows the voltage time histories for different λ_0 values, computed the same way as Figure 5. Increasing λ with all other parameters fixed, we see that voltage variance decreases. This is consistent with the constant mean flux case where $\sigma_V \rightarrow 0$ as $\lambda \rightarrow \infty$.

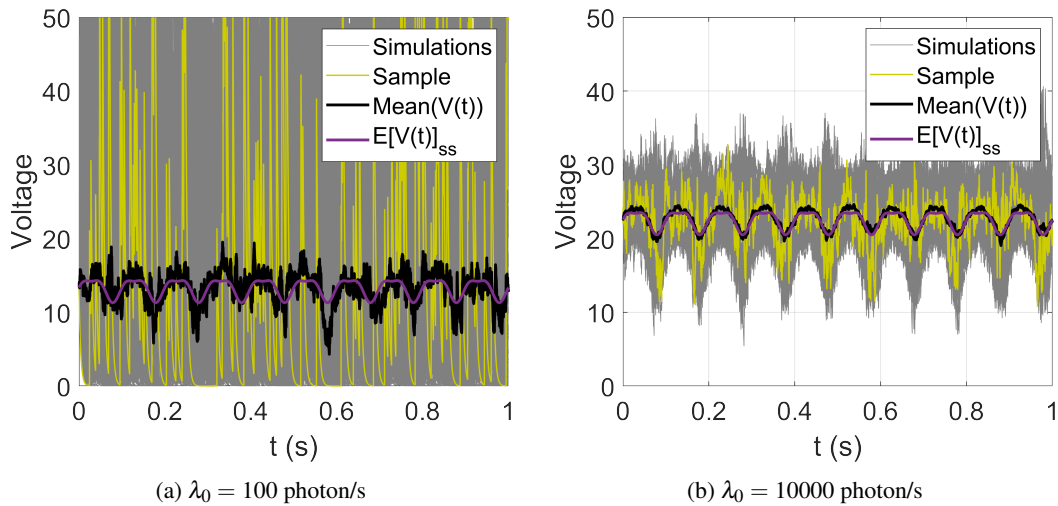


Fig. 6: Voltage for 10 Hz $\lambda(t)$ sinusoid with $\lambda_1/\lambda_0 = 0.75$ ($\Delta m \sim 2$), $a = 250$, $b = 500$, $\Delta\bar{\lambda} = 10\%$, 100 runs each

With the Figure 6 results in mind, we now turn to the scenario where λ_0 is large enough that it closely tracks $E[V(t)]_{ss}$. This will allow us to explore frequency estimation dependencies in a deterministic sense using Eq. 14. Again, the two parameters dictating the voltage amplitude and the resulting event rates for $E[V(t)]_{ss}$ are λ_1/λ_0 and ω/a .

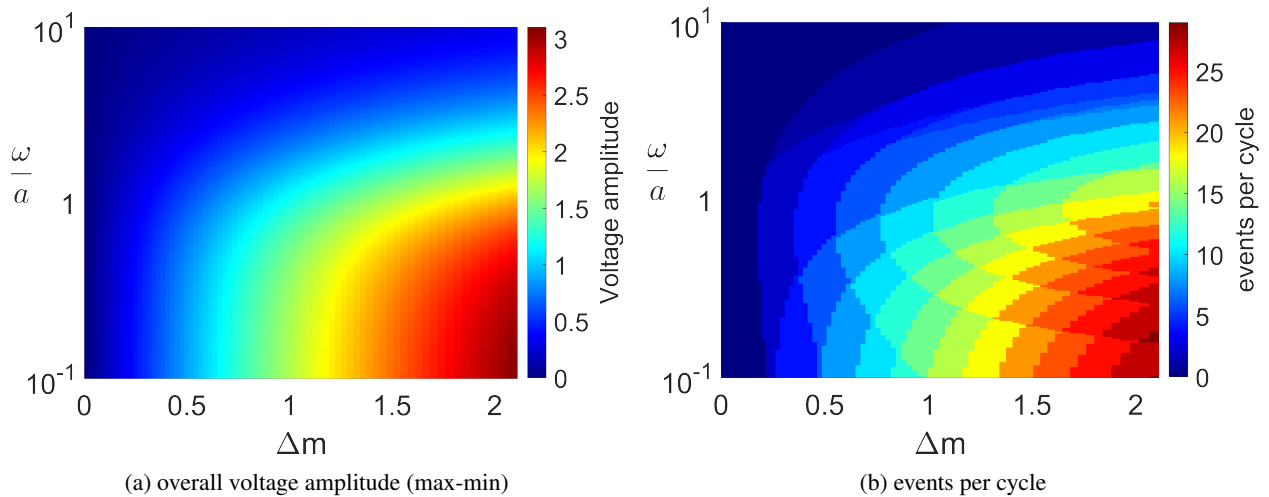


Fig. 7: $E[V(t)]_{ss}$ event analysis for $\Delta\bar{\lambda} = 10\%$

Figure 7 shows plots of the overall voltage amplitude (neglecting b/a) and the number of events per cycle. The larger the voltage amplitude, the higher the number of events per cycle. More signal-driven events will yield better frequency estimate SNR. The event calculation assumes that the camera clock speed is much faster than ω so that all possible events are detected. Unsurprisingly, as we increase the $\lambda(t)$ amplitude, given here as the magnitude change Δm , the voltage amplitude and event counts increase. Then for $\omega \ll a$, the event circuit reacts quickly enough to track the $\lambda(t)$ oscillation. As ω/a increases, the voltage amplitude decreases as the circuit has a harder time keeping up with the oscillation. Finally, for $\omega \gg a$, the circuit becomes unresponsive to oscillation. So overall, slower $\lambda(t)$ variation with larger amplitude should yield higher SNR frequency estimates from the event data.

3.3 Moving Point Sources

We will now consider the case where the point source moves across the sensor field of view at a constant velocity. To compute the time-varying $\lambda_{ij}(t)$, we set $\bar{x}(t) = \dot{\bar{x}}t + \bar{x}_0$ and $\bar{y}(t) = \dot{\bar{y}}t + \bar{y}_0$ in Eq. 15. For bright, fast-moving point sources, the voltage response will be dominated by motion rather than shot noise. So instead of simulating Eq. 4 with an NHPP, we numerically integrate Eq. 7 to solve for the mean voltage response. Numerical integration is also more efficient for bright sources where many billions of photon hits would need to be simulated.

Figure 8 shows the resulting event time histories for different target magnitudes and velocities. In all cases, the point source is moving to the right and the time resolution for events is set to $10 \mu s$. We assume a 0.2 m aperture $f/3$ telescope with $4.9 \times 4.9 \mu m$ pixels to approximate the sensor configuration used to collect real observations (see the next section). To better compare with collected data, we also compute the PSF using the seeing diameter (assuming a FWHM of 6 arcsec). Starting with the left column of Figure 8, we show results for a $1 m_v$ source. Here we plot the net sum of events over 100 time steps (1 ms) with white regions denoting net positive events (i.e. increase in voltage) and blue regions denoting net negative events (decrease in voltage). Given the rightward motion, there are positive events to the right and negative events to the left. These regions correspond to the leading and trailing edges of the PSF respectively. So the event data explicitly indicate the direction of motion.

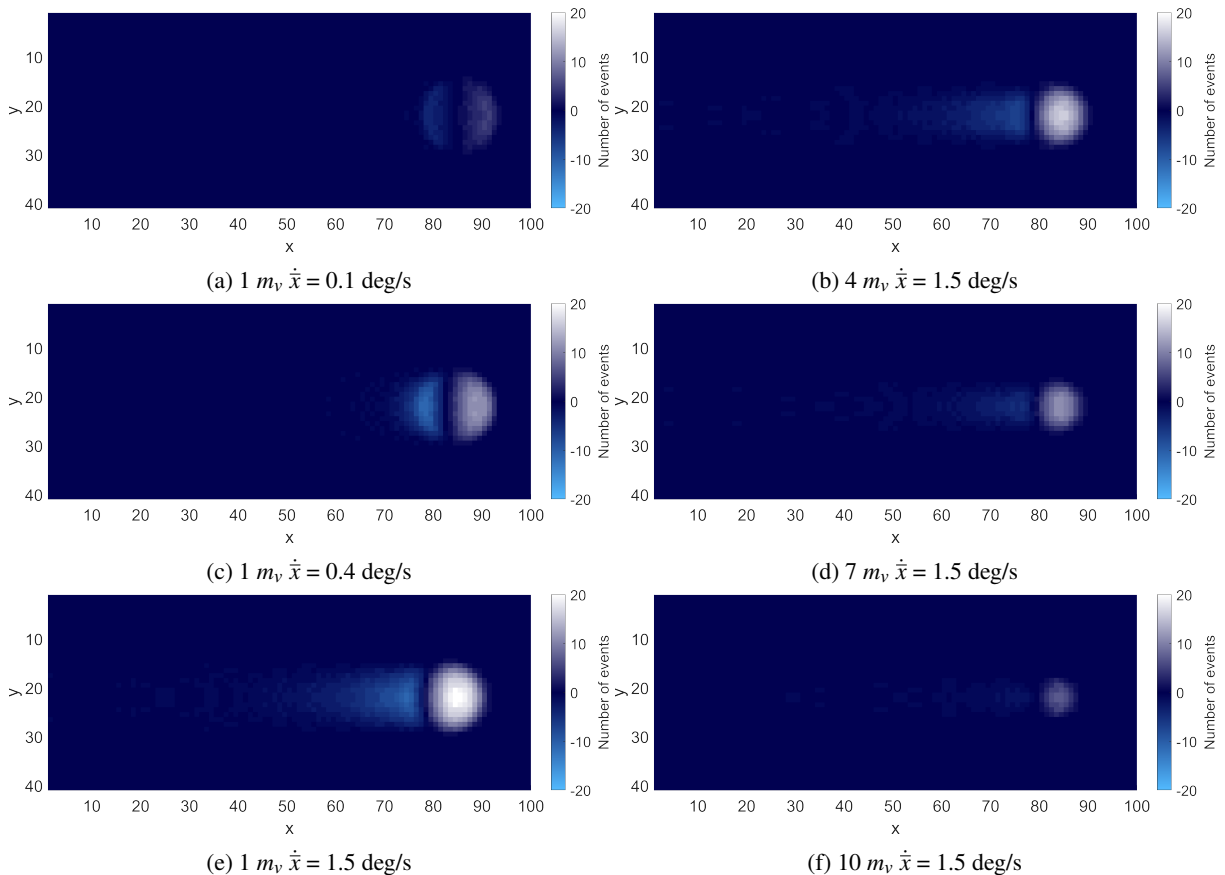


Fig. 8: Net event sum over 1 ms (100 time steps) for moving point sources with $a = 250$, $b = 500$, $\Delta\bar{\lambda} = 10\%$

Increasing the PSF velocity, we notice two prominent trends: 1) enhancement of the leading edge "bow shock" and 2) lengthening of the decay tail. The bow shock intensity increases because the voltage ramps up more rapidly for faster PSF motion. With the PSF moving faster, the decay tail also grows because the voltage in a given pixel has had less time to decay. This tail structure is further illustrated by Figure 9a where we show the pixel voltages along the centerline of the PSF at the same time step shown in Figure 8. Here, the voltage tail grows with increasing PSF velocity. We also see that the peak voltage is higher for slower velocities because the voltage has more time to approach steady state before λ drops. It is also important to note that while the slope of the voltage vs. pixel curve is highest for the slowest PSF in Figure 9a, it is the voltage time derivative in a given pixel that determines event rates.

Overall, the near-instantaneous event structure is quite sensitive to the target's velocity. With the PSF leading edge impinging on undisturbed pixels, the bow shock intensity is more sensitive to instantaneous changes in velocity than the tail. The tail structure on the other hand depends more on the rate history due to the PSF having traversed all of the underlying pixels. Figures 8a,c,e and Figure 9a also show that the bow shock and peak voltage move farther leftward the faster the PSF moves. Figure 9b shows the pixel flux at the same instant as the event and voltage plots and it is nearly aligned with the slowest PSF case. So the faster motion also causes more lag in both the voltage response and the perceived location of the point source in the event data. From an astrometry perspective, this has significant implications for along-track position estimation because the bow shock may trail the PSF centroid. It is important to note that the near-instantaneous velocity information encoded in these event "freeze frames" is supplemented by the time-varying position of the event streak in the field of view, which can also be used to obtain velocity information (as with traditional exposure-based sensors).

We also include event histories for dimmer point sources in Figures 8b,d,f. Compared with the $1 m_v$ case in Figure 8e with the same velocity, the bow shock weakens and the tail shortens with decreasing brightness. This is because the peak voltages decrease, resulting in fewer and fewer total events.

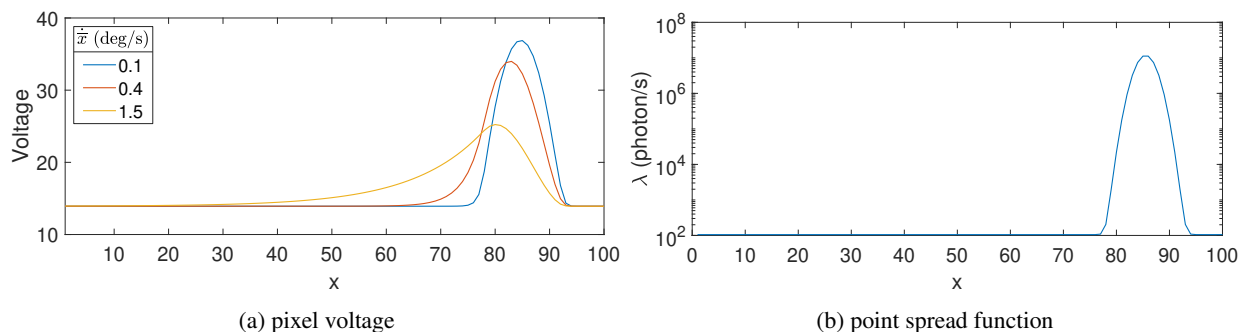


Fig. 9: Pixel voltage and flux along PSF motion centerline corresponding to the $1 m_v$ source in Figures 8a,c,e

4. OBSERVATION CAMPAIGNS

4.1 Data Collection

The event data presented in this work were collected at the observatory on the University of Colorado Boulder's Aerospace Engineering building. The observatory dome, shown in Figure 10, houses a set of four co-aligned Officina Stellare RH200 0.2 m f/3 telescopes (visible in Figure 10) fixed to a Planewave L-600 mount. The event camera optical train consists of one of these RH200's, an FLI Atlas focuser, and a Prophesee EVK3 HD (i.e. GEN 4.1) with a 1280×720 array and $4.86 \times 4.86 \mu\text{m}$ pixels. The EVK3 outputs a stream of events comprised of (x, y) pixel location, \pm event polarity, and timestamps with $1 \mu\text{s}$ resolution. Unlike some event cameras, the EVK3 does not output simultaneous intensity measurements [5]. This reduced pixel complexity is partially responsible for the EVK3 HD having the smallest pixel pitch and highest fill factor (77%) of commercially available event cameras [5]. For the RH200, this pixel size results in an instantaneous field of view (IFOV) of 1.67 arcsec/pixel. Mount pointing was conducted with Planewave's PWI4 software and the event data were acquired with Prophesee's Metavision Intelligence software suite.



Fig. 10: Campus observatory with four co-aligned Officina Stellare RH200 0.2 m telescopes

4.2 Static Sources

We will start with observations of fixed sources. We focused the telescope by minimizing the angular size of dim stars in the event data. The donut structure of out of focus stars mimics that of Poisson-driven event depressions. Figure 11 shows the event counts for the focused $1.3 m_v$ star Regulus at three different times accumulated over 0.25 s. For each plot, the pixel event counts initially increase moving towards the center, but at the center we see a decrease in events. This general structure is consistent with our simulation results in Figures 3 and 4. We also see comparable peak event rates (~ 1000 events/s). We should note that the circuit parameters used in the simulated results are almost certainly different from the true circuit's values. This likely explains in part why the reduction in events at the center of Regulus' PSF is not more dramatic. For example, varying a in Figure 2 changes the shape of the λ vs. event rate curve and the resulting depth of the event depression for bright sources. At the same time, it is likely that atmospheric seeing disrupts the pure shot noise driven behavior of our model, resulting in flux variations that increase the event rate. Reducing the event accumulation time to 0.1 and 0.05 s to better "freeze" atmospheric turbulence resulted in somewhat reduced central event rates relative to the rim, supporting this hypothesis. Overall, it would be valuable to observe Regulus and other bright stars with better seeing to determine whether these results change.

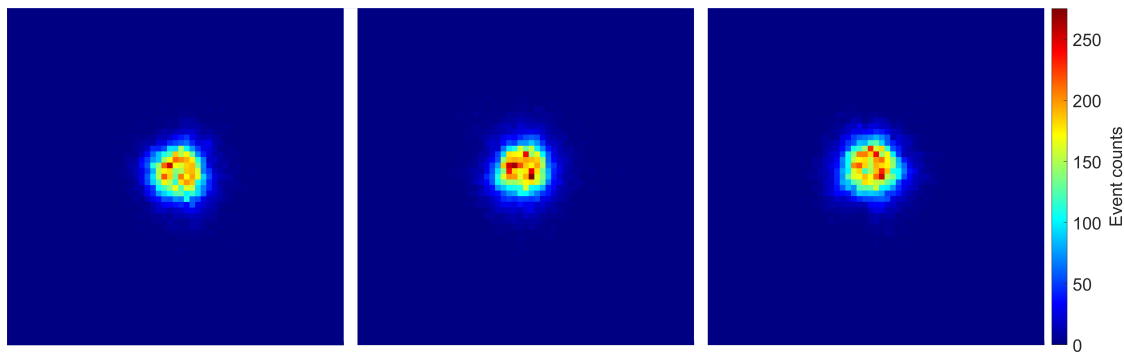


Fig. 11: Event counts over 0.25 s at three instances for the focused $1.3 m_v$ star Regulus (May 11, 2022)

Figure 12 shows event counts for the Jupiter and Saturn systems accumulated over 1 s. For the Jupiter system, we see from left to right: Io, Jupiter, Europa, Callisto, and Ganymede. For the Saturn system, all the visible moons are in roughly a straight line. From left to right we have: Titan, Rhea, Saturn, Tethys, and Dione. The object directly below Rhea in the bottom center is $8.6 m_v$ star HD205926. Both Jupiter and Saturn ($-2.6 m_v$ and $0.3 m_v$ respectively) have more substantial event depressions than Regulus, with no events at their centers where they are the brightest. This indicates that the relative flux variation due to shot noise and seeing is insufficient to generate events. Moving outward from the center, the event rates increase. This indicates larger relative flux variation, likely due to lower brightness along Jupiter's limb and in Saturn's rings. While Jupiter and Saturn are resolved, these observations are consistent with the event depression structure in the Figure 3 and 4 point source simulations. Unlike Regulus, Jupiter, and Saturn, the moons and HD205926 have no event depressions likely due to a combination of the maximum pixel flux lying below

the event rate peak as well as seeing, which causes high relative fluctuations in the brightest pixels. For the moons and other dim point sources to have event depressions, assuming diffraction-limited observing, our models indicate that one would need high angular resolution to push λ_{ij} corresponding to the peak event rate outward as well as a sufficiently large collecting area so that flux at the center is past the event rate peak.

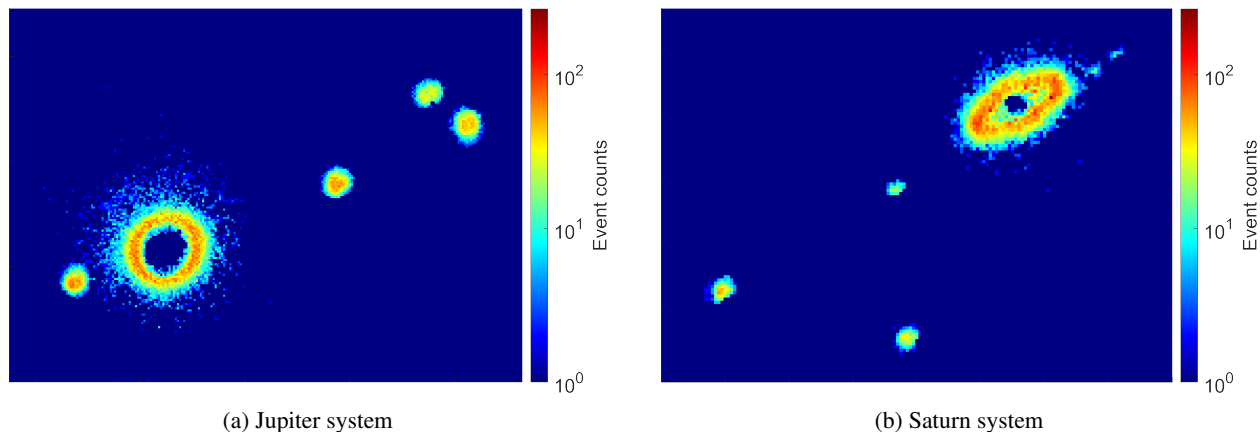


Fig. 12: Event observations of the Jupiter and Saturn systems on Aug. 9, 2022 with 1 s event accumulation.

4.3 Moving Point Sources

We will now explore event data for point sources moving across the field of view. Figure 13 shows the net event sum when slewing to the $1 m_v$ star Pollux. In this scenario, the initial slew rate was ~ 2 deg/s and the velocity slowed rapidly as pointing converged. With the star moving to the right, Figure 13 shows the event structure at three successive times where the star had a high, medium, and low velocity. For each 100×40 pixel frame, events were accumulated for 1 ms and all frames have the same event sum color bounds. Moving from high to low velocity we see both a general decrease in bow shock intensity and tail length. This indicates a decrease in the event rate at the bow shock for slower speeds due to the slower voltage ramp as well as lower tail voltage due to longer decay time after the PSF has passed. Overall, these results are consistent with the Figure 8a,c,e simulations.

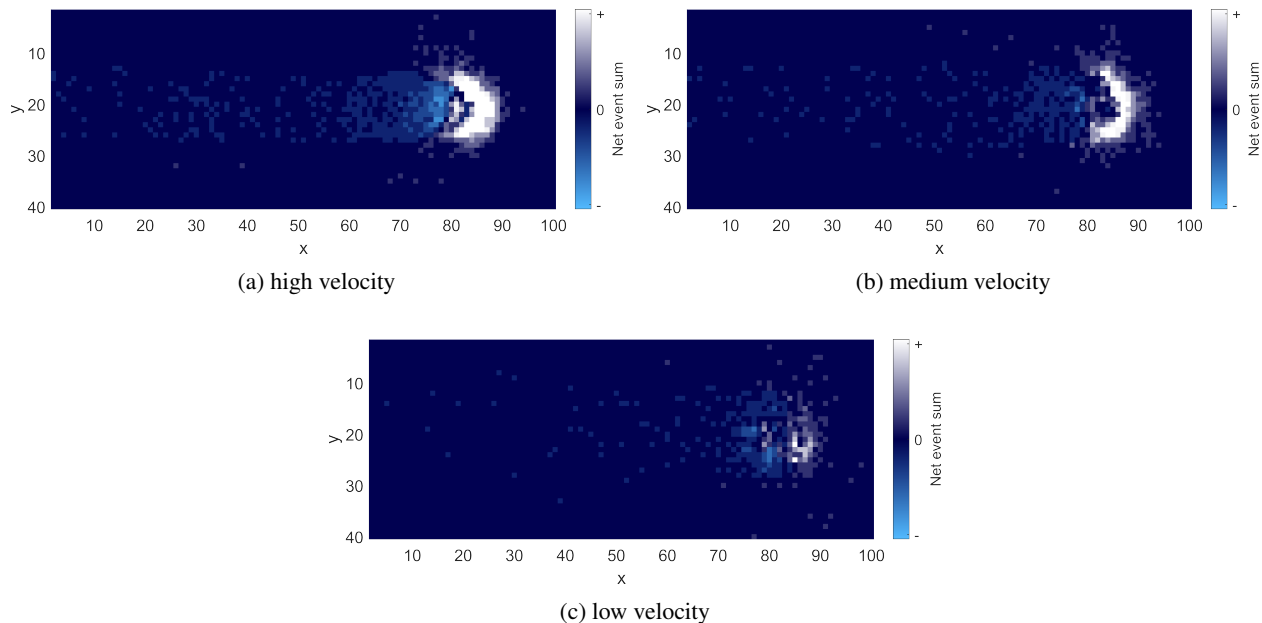


Fig. 13: Event structure for a decelerating slew to the $1 m_v$ star Pollux on May 11, 2022 (1 ms event accumulation)

Figure 14 shows the net accumulation of events over 0.5 s when rate-tracking the GEO satellites AMC-21 and Galaxy 30. The satellites have (x,y) pixel indices of $(820,390)$ and $(1030,490)$ respectively. AMC-21 has notably more events than Galaxy 30. The other objects are trailing field stars of varying brightness. The brighter stars generate larger bow shocks and longer tails. This is consistent with the results from Figure 8.

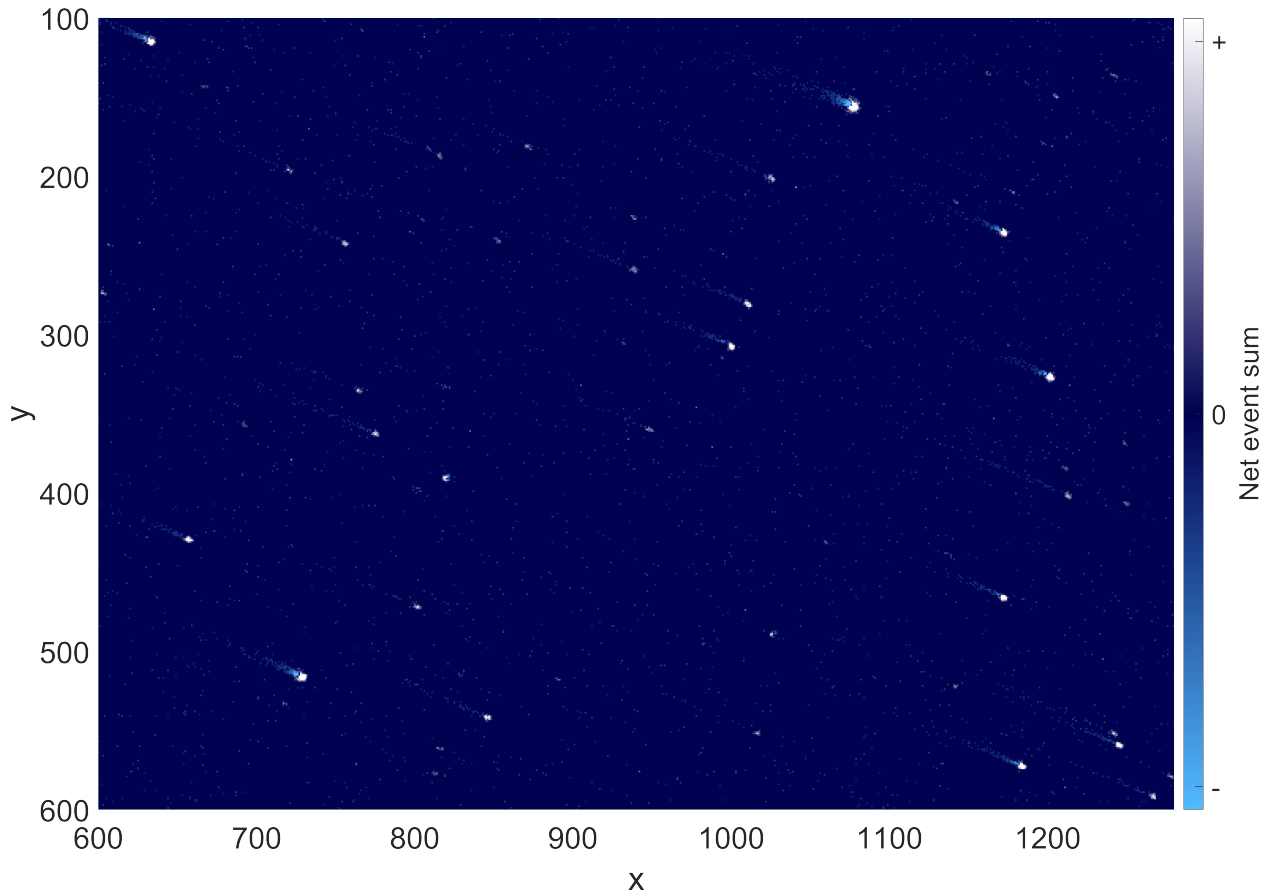


Fig. 14: Net event sum over 0.5 s when tracking GEO satellites AMC-21 and Galaxy 30 (Aug. 22, 2022)

4.4 Event Data Frequency Analysis

We will now analyze event data for its frequency content. We will start with Ajisai, a Japanese LEO satellite used for precise geodetic positioning. In addition to retro-reflectors for laser ranging, the spherical Ajisai satellite is covered in roughly 300 mirrors which provide an average of 3 - 6 glints per rotation [12, 6, 7]. The satellite was launched in 1986 with a rotation period of 1.4 s and spin axis aligned with the negative celestial pole [12]. Due to environmental perturbations, the satellite is slowly decelerating and had a spin period of ~ 2.4 s in 2020 [7]. This rapid rotation and the frequent glints makes Ajisai an intriguing target for event camera study.

Figure 15 shows the mean event time history over 15.1 s when rate-tracking Ajisai. To analyze the event data, we selected pixels at the center of the event structure where the event counts were highest. Figure 15a shows the resulting mean event time history over the central 7×6 pixels. The event spikes generally correspond to brief glints. Phase-folding the mean event history over a range of candidate synodic (i.e. apparent) periods, Figure 15b show the solution for the best-fit period of 2.541 s. Notably poorer glint alignment was observed for deviations of only several milliseconds. This best-fit synodic period is consistent with Ajisai's continued deceleration since 2020.

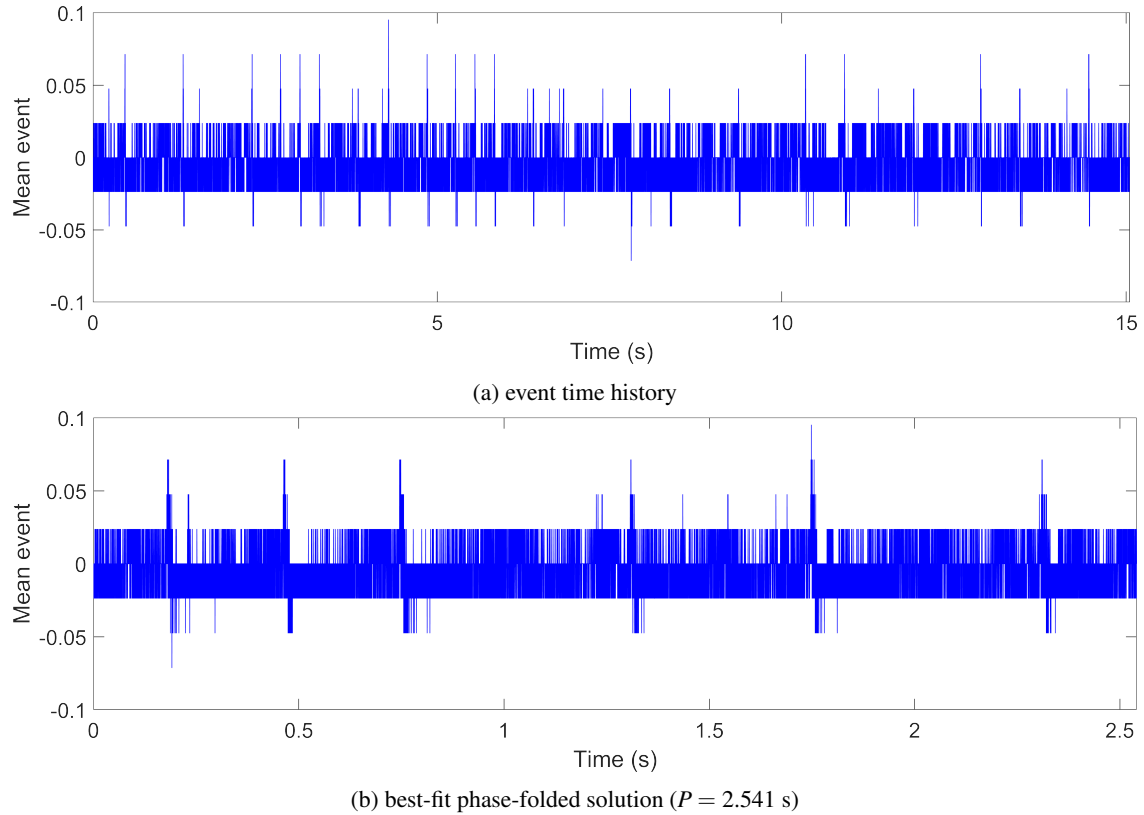


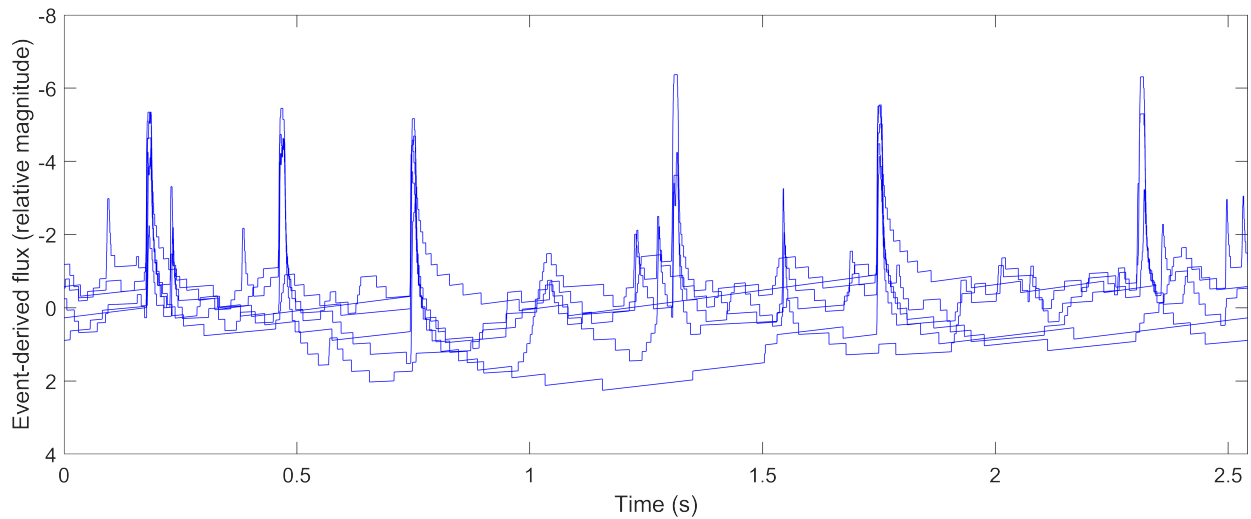
Fig. 15: Mean event time history over 7×6 pixels for Ajisai (Aug. 9, 2022)

From the event time history, we can also generate event-derived light curves. In the ideal noise-free case, events are only declared when the relative change in pixel flux exceeds $\pm\Delta\bar{\lambda}$. So starting at the initial time t_0 with flux $\lambda(t_0)$, we sequentially compute the pixel fluxes $\lambda(t_{i+1})$ relative to $\lambda(t_i)$. To compute $\lambda(t_{i+1})$ we multiply $\lambda(t_i)$ by $(1 + p \Delta\bar{\lambda})$ for each event between t_i and t_{i+1} where p is the event polarity (i.e. + or -). Note that this approach assumes the pixel flux has changed by exactly $\pm\Delta\bar{\lambda}$ at the event time, which is likely not strictly true. If there are no events between t_i and t_{i+1} , we hold the flux constant. We can then convert these relative absolute fluxes to relative magnitudes ($m_i = -2.5 \log_{10}(\lambda_i/\lambda_0)$). Finally, we detrend the event-derived flux magnitudes with a polynomial fit to remove effects of: 1) changing mean magnitude due to time-varying observation geometry, 2) event noise, and 3) the possibility of event asymmetry (e.g. more negative events than positive for cycle as with Figure 5 analysis above).

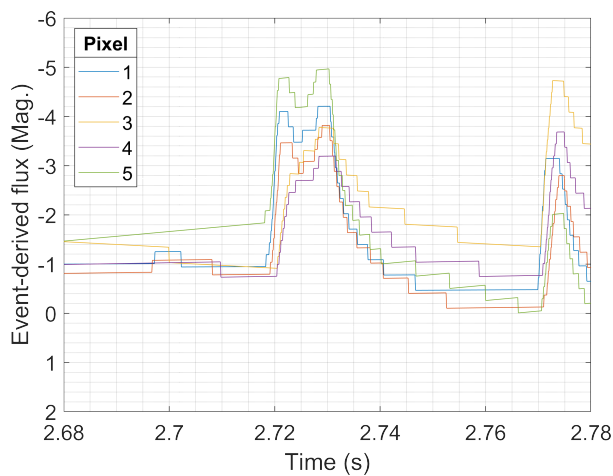
Figure 16a shows the resulting event-derived light curve for the highest event count pixel from the Figure 15 track. Here we compute m_i at 0.1 ms intervals and use the default EVK3 event threshold $\Delta\bar{\lambda}$ (nominally $\pm 25\%$). We detrended the light curve with a 2nd order polynomial fit. The Figure 16a event light curve is folded on the best-fit period of 2.542 s. First of all, we see an amplitude of roughly 6 magnitudes. This is consistent with the ~ 6 magnitude variation observed in traditional exposure-based Ajisai light curves [6]. We also see six bright glints per cycle as well as other dimmer ones. Previous exposure-based and photon counter studies also found an average of 3-6 glints per cycle [6, 7].

Figure 16b and c show zoomed in views of two glints captured by the event light curves for the five highest event count pixels. Note that the time here is chronological rather than phase-folded, so the five curves are at the same instants in time. For both glints, we see a maximum glint width of ~ 10 ms. Using a photon counter, Kucharski et al. [7] observed an averaged Ajisai glint FWHM of 10.3 ms. For the glint in Figure 16b, three of the five pixels show a dip in flux on the glint plateau. Similar dips were observed for other glints. These dips are consistent with impact-driven mirror degradation observed by Kucharski et al. They found that mirrors at intermediate latitudes relative to Ajisai's equator tended to have the most degradation due to preferential impacts from these directions. For the Aug. 9, 2022 track, our observation geometry viewed Ajisai at high latitudes, so the Figure 16 glints are from the intermediate latitude

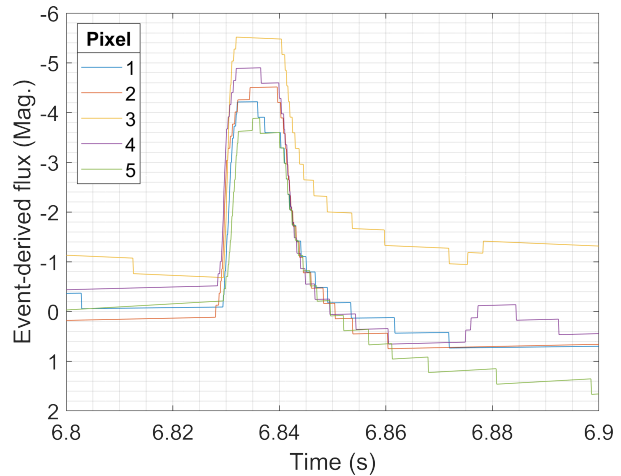
mirrors. In Figure 16c, the glint peaks correspond to a different mirror since the time difference is not a multiple of the rotation period. The glints are much flatter, consistent with the mirror to mirror variation observed by Kucharski et al. It is also worthy to note that the glint profiles in Figure 16 are asymmetric with the rising edge sharper than the falling edge. For the photon counter data, the glints are symmetric [7]. This discrepancy is likely due to non-instantaneous voltage decay in the event camera pixels.



(a) phase-folded event-derived light curve for the highest event count pixel ($P = 2.542$ s)



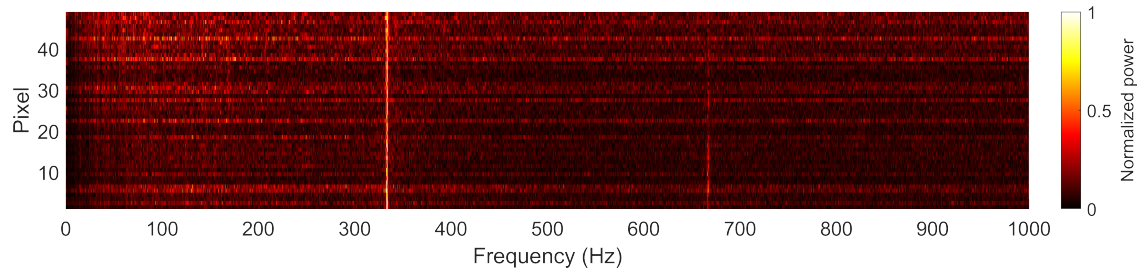
(b) irregular glint



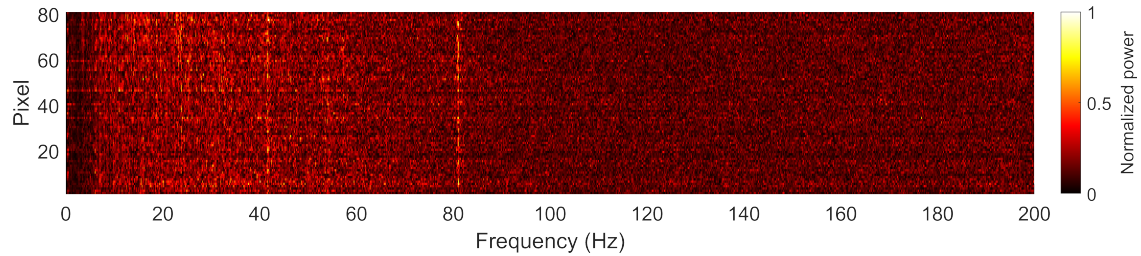
(c) flat glint

Fig. 16: Ajisai event-derived light curve (Aug. 9, 2022)

Figure 17 shows the event data frequency spectra for the bright stars Regulus and Castor. Here we compute the FFTs of the raw event time histories for each of the central pixels independently. The pixels are ordered by decreasing event count (i.e. pixel 1 has the most events). For Regulus we see a primary peak across all pixels at 333 Hz. The higher event pixels also have the second harmonic. For Castor, the primary peak is much lower, at 81 Hz with a notable subharmonic at 40 Hz. For Castor, there were no prominent frequencies above 81 Hz. On short timescales, we would expect brightness variations to be driven by seeing. The frequency of these variations is roughly on the order of 100 Hz, which is more consistent with the Castor primary frequency. Interestingly though, the primary frequencies for Castor and Regulus differ by almost exactly a factor of four. So it is possible that the atmospheric fluctuation rate on the two nights were similar and we are just seeing different harmonics. Alternatively, these frequencies could be driven by the event camera circuit (e.g. the voltage decay rate), as very similar frequencies were also observed for a number of other natural and artificial objects on different nights.



(a) 1.3 m_v Regulus (May 11, 2022, 2 s FFT integration)



(b) 1.6 m_v Castor (May 15, 2022, 5 s FFT integration)

Fig. 17: Raw event data frequency spectra for two stars

Figure 18 shows the event counts for the International Space Station (ISS) on May 15, 2022. At the time of these observations, the ISS was at a range of 550 km. Given its ~ 100 m length and foreshortening, we would expect the ISS to cover roughly 20×20 pixels for our 1.67 arcsec IFOV. This is roughly what we see in Figure 18. The solar arrays and central section of the ISS are coarsely resolved. The middle of these features have relatively few events. This is likely due to the high brightness in these pixels and the low relative flux variation.

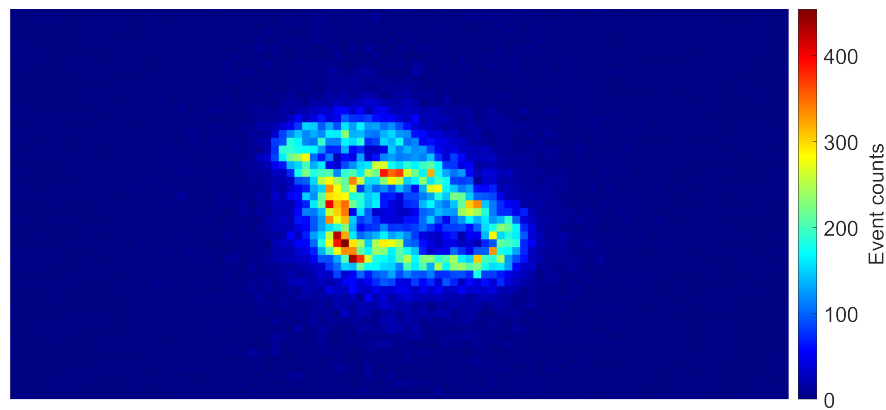


Fig. 18: International Space Station event counts over 1 s (May 15, 2022)

Figure 19 shows event data frequency spectra for the ISS. Here we plot the spectra over four consecutive 2 s intervals for comparison. Again, the pixels are ordered in terms of decreasing event count. As with the Castor observations, taken less than an hour earlier on the same night, we see prominent peaks at ~ 42 and ~ 82 Hz which are likely due to seeing or the event camera circuit. We also see notable peaks at ~ 10 and ~ 13 Hz for the first and fourth plots. These are not present in the Castor or Regulus spectra. The ISS's Ku-band communications antenna is known to induce vibrations at 10.6 and 13.1 Hz while slewing [10]. This antenna is the primary source of ISS vibrations in the 5 - 20 Hz range [10]. So it is possible that these observed event signatures are due to the antenna. The intensity of antenna-induced vibrations varies with time [10], potentially explaining the disappearance of these ~ 10 and ~ 13 Hz peaks in the middle two plots. It is also possible that the signatures are subharmonics ($\sim 1/4$ and $\sim 1/3$) of the ~ 42 Hz primary frequency. Further investigation is needed to determine the sources of these various signatures.

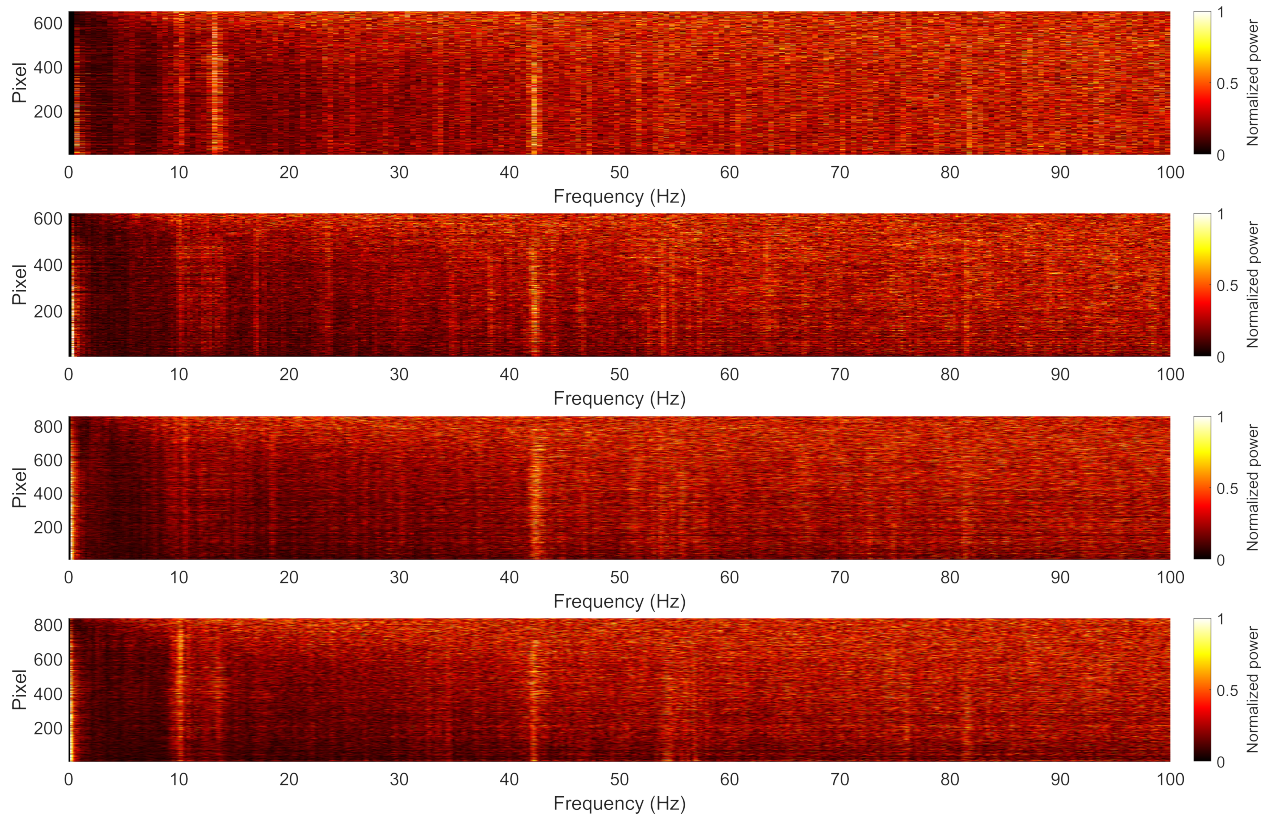


Fig. 19: ISS raw event data frequency spectra over four consecutive 2 s intervals (May 15, 2022)

5. CONCLUSIONS

In this paper, we presented a stochastic event camera model for non-resolved objects. Comparisons between simulated and real event camera observations of static and moving sources showed clear consistencies. The presented model improves our fundamental understanding of event data for non-resolved objects and facilitates matched filter template generation for object detection, tracking, and characterization. For static point sources, we observed a clear relationship between mean brightness and event structure. Our modeling suggests that shot noise and logarithmic flux dependence should allow for detection of sufficiently bright stars when sidereally tracking even in the absence of atmospheric turbulence or jitter. This strengthens the promise of using event cameras for sidereally-tracked modes of operation where objects streak through the field of view with background stars providing inertial reference. For moving sources, we found that the event bow shock and tail shapes are sensitive to near-instantaneous rates and brightness. This demonstrates the potential to extract high resolution position and near-instantaneous rate information from event data. Such capabilities would offer significant astrometric advancements. We also explored event camera simulations for sources with sinusoidal mean brightness variations, illustrating the complex dependence of frequency estimates on the target brightness amplitude and variation frequency as well as the event circuit parameters. For the real Aji-sai observations, we also demonstrated the ability to extract high-rate photometric information from event data that is consistent with previous exposure-based and photon counter results. Overall, the simulated and observed results demonstrate the great potential of event data for high spatial and temporal resolution space domain awareness studies.

In terms of future work, further development is needed to extend analytical solutions for voltage statistics to event rate statistics. Analytical event rate solutions will be especially useful for modeling bright point sources. Also, additional observations are needed to further validate the simulated event depression structure for point sources. This could be accomplished by observing stars using a larger aperture telescope with higher angular resolution and in better seeing conditions to minimize turbulence effects. Also, for event data frequency analysis, further study is needed to isolate target-driven signatures from those induced by the event circuit and environment.

6. ACKNOWLEDGEMENTS

We would like to acknowledge L3Harris for funding this research. We would also like to thank Samuel Fedeler, Casey Heidrich, Michael Klonowski, Patrick Miga, and the CU Aerospace machine shop for assisting with development and testing of the telescope system used in this work. Finally, we would like to thank Dave Monet for his event camera insights and suggestions.

7. REFERENCES

- [1] R. D. Coder and M. J. Holzinger. Multi-objective design of optical systems for space situational awareness. *Acta Astronautica*, 128, 2016.
- [2] G. Cohen, S. Afshar, and A. van Schaik. Approaches for astrometry using event-based sensors. *Proceedings of the 19th AMOS Conference*, 2018.
- [3] G. Cohen et al. Event-based sensing for space situational awareness. *The Journal of the Astronautical Sciences*, 66:125–141, 2019.
- [4] R. Durrett. *Essentials in Stochastic Processes*. Springer New York, NY, 2nd edition, 2012.
- [5] G. Gallego et al. Event-based vision: A survey. *IEEE Transactions on Pattern Analysis and Machine Intelligence*, 44(1), 2020.
- [6] N. Koshkin, L. Shakun, N. Burlak, E. Korobeynikova, S. Strakhova, S. Melikyants, S. Terpan, and A. Ryabov. Ajsai spin-axis precession and rotation-period variations from photometric observations. *Advances in Space Research*, 60(7), 2017.
- [7] D. Kucharski, G. Kirchner, T. Otsubo, S. K. Flegel, H. Kunimori, M. K. Jah, F. Koidl, J. C. Bennett, M. Steindorfer, and P. Wang. Quanta photogrammetry of experimental geodetic satellite for remote detection of micrometeoroid and orbital debris impacts. *Acta Astronautica*, 174, 2020.
- [8] P. Lichtsteiner, C. Posch, and T. Delbruck. A 128x128 120 db 15 μ s latency asynchronous temporal contrast vision sensor. *IEEE Journal of Solid State Circuits*, 43(2), 2008.
- [9] P. N. McMahon-Crabtree and D. G. Monet. Commercial-off-the-shelf event-based cameras for space surveillance applications. *Applied Optics*, 60(25), 2021.
- [10] K. McPherson, K. Hrovat, E. Kelly, and J. Keller. A researcher’s guide to: International space station acceleration environment. *NASA ISS Program Science Office*, 2015.
- [11] R. Pasupathy. Generating homogeneous poisson processes. *Wiley encyclopedia of operations research and management science*, 2010.
- [12] M. Sasaki and H. Hashimoto. Launch and observation program of the experimental geodetic satellite of japan. *IEEE Transactions on Geoscience and Remote Sensing*, 25(5), 1987.
- [13] J. R. Shell. Optimizing orbital debris monitoring with optical telescopes. *Proceedings of the 19th AMOS Conference*, 2010.
- [14] J. Spurbeck, M. K. Jah, D. Kucharski, J. C. S. Bennett, and James G. Webb. Near real time satellite event detection, characterization, and operational assessment via the exploitation of remote photoacoustic signatures. *The Journal of the Astronautical Sciences*, 68:197–224, 2021.